Hindawi
International Journal of Aerospace Engineering
Volume 2022, Article ID 5474763, 13 pages
https://doi.org/10.1155/2022/5474763

Research Article

Numerical Study on Effects of Arrayed Pulsed Energy Depositions on a Supersonic Combustor

Zilin Cai,[1] Feng Gao,[1] Hongyu Wang,[2] and Cenrui Ma[1]

[1]*Air and Missile Defense College, Air Force Engineering University, Xi'an 710051, China*
[2]*Hypervelocity Aerodynamics Institute, China Aerodynamics Research and Development Center, Mianyang 621000, China*

Correspondence should be addressed to Hongyu Wang; wanghongyu@cardc.cn

Received 23 June 2022; Revised 25 July 2022; Accepted 11 August 2022; Published 20 October 2022

Academic Editor: Jun-Wei Li

This paper proposes a method to improve the mixing efficiency of a supersonic combustor by using arrayed pulsed energy depositions, and this method is verified by a numerical simulation. In the simulation, the Navier-Stokes equations with an energy source are solved to simulate the effects of energy depositions in various distributions on the fuel mixture in the combustor. It is found that the energy deposition arranged in the streamwise direction leads to a significant improvement in the mixing efficiency and maximum concentration decay rate of the ethylene fuel by increasing the scale of the jet-induced counter-rotating vortex pair. The energy deposition arranged in the spanwise direction introduces another counter-rotating vortex pair which can also contribute to the fuel mixture. By comparison, the energy deposition distributed in the streamwise direction and downstream of the jet orifice is shown to be the most effective case in the fuel mixing enhancement. Under the energy deposition, the wall pressure on the trailing edge of the cavity is increased which leads to a decrease in the total pressure recovery of the combustor, but this decrease is not significant.

1. Introduction

As one of the new types of advanced engines, scramjet has a wide range of promising applications in areas such as hypersonic cruise missiles, hypersonic aircraft, and aerospace vehicles. The scramjet's internal flow has an extremely high speed, resulting in a very short fuel-residence time. Therefore, a key issue in the design of a scramjet is how to ensure adequate mixing and combustion of the fuel in such a short time, which has attracted much attention in recent years.

Researchers have conducted extensive studies on potential ways of improving fuel mixing efficiency, by employing the active and passive flow control techniques inside a supersonic combustor, such as all kinds of struts, steps, pulsed jets, cavities, aerodynamic ramps, pylons, transverse injectors, and the cantilevered ramp injector [1–5]. The concept of their combinations has also attracted widespread attention. One popular technique to improve mixing efficiency is to introduce streamwise vortexes in the flow. This can promote momentum exchange between the fuel and the main flow and also increase the penetration depth of the fuel [6–8]. Some common mixing enhancement methods are listed in Table 1.

Extensive research [9, 10] showed that a cavity, combined with a transverse fuel injection upstream of it, can promote combustion and flame stabilization within the supersonic combustor. This combination style for combustion, however, makes it difficult for the fuel to reach adequate mixing in supersonic flows with a large momentum. Therefore, some mechanical devices, mentioned above, are often applied to enhance fuel mixing. This will, however, bring loss to the total pressure recovery of the scramjet. Some alternative methods are desperately needed for mixing improvement purpose with the least penalties.

The plasma energy deposition, as one of the active flow control methods, seems to be rather promising, which has aroused widespread interest in recent years. The energy depositions can be realized by a variety of discharges,

including pulsed ones (known as nanosecond/microsecond pulsed discharges) or steady ones (known as quasidirect current discharges). These discharges are characterized by a quick response time, high intensity, and wide frequency bandwidth. Their operating states can be flexibly adjusted according to the incoming flow conditions. Since the actuators based on energy deposition generally do not intrude into the flow, a large total pressure loss can be avoided that may be caused by some intrusive mechanical devices. Leonov et al. [11] used high-resolution imaging to capture the evolution process of a quasi-DC discharge plasma energy deposition in a high-speed flow. Their experimental results demonstrated that the extremely fast turbulent expansion induced by the discharge positively contributes to the mixing of nonpremixed multicomponent flows. Leonov et al. and Houpt et al. [12, 13] also studied the effect of quasi-DC discharge on fuel mixing in a supersonic combustor with a cavity. It was found that the oblique shock wave induced by the thermal choking effect of discharge not only enhances the mixing of the fuel in the shear layer but also increases the pressure in the cavity, which contributes to fuel combustion. Shi et al. [14] studied the effects of a pulsed discharge on the control of mixing in a circular tube-free jet. Their results showed that the pulsed discharge at a certain frequency effectively promotes the development of the large-scale structures of the jet's shear layer. It was also found that when the discharge is located above the jet, it is more beneficial to the formation and development of the large-scale vortex structures, and this allows for a better mixing efficiency. Ombrello et al. [15] experimentally studied the interactions between a pulsed discharge and a supersonic jet and found that the position of the discharge actuator has a considerable effect on the jet mixing and that there is an optimal actuation position. Rogg et al. [16] studied the effects of laser energy depositions on the mixing in a supersonic combustor. It is concluded that the energy depositions with repetitive frequencies are more effective than that of a single pulse. By using a numerical simulation, Zheltovodov and Pimonov [17] revealed a mixing enhancement caused by the interaction between pulsed energy depositions and a supersonic jet. They also found that the energy deposition position relative to the jet is a key factor to form large-scale vortexes that enhance the mixing. Recently, Liu et al. [18] investigated the mixing enhancement mechanism of a supersonic circular tube jet under a pulsed energy deposition. Their results showed that the energy deposition is more effective in mixing enhancement when it is located inside the jet.

In recent years, arrayed pulsed energy depositions based on nanosecond/microsecond pulsed discharges have been attempted for high-speed flow controls [19, 20], which are considered potential approaches to improve supersonic flow qualities. They can induce consistently heated gases that propagate downstream and are gradually expanding during their propagation. The perturbations of these heated gases can change the shock wave structures in a supersonic flow. These structures possibly exert severe disturbances to a jet-induced flow. In a supersonic combustor, if these heated gases are interacting with a transverse fuel jet, some fresh phenomena and coupling effects will be introduced that may contribute to the fuel mixture. To verify this assumption, this study will numerically explore the effects of arrayed pulsed energy depositions on the fuel mixture of a supersonic combustor. An energy source term is added to the energy equation to simulate the heating process of the energy deposition. Different distributions of the energy deposition are arranged in this study to ensure a comparative analysis.

Table 1: Some common mixing enhancement methods [1–5].

Active ones	Passive ones
Pulsed jet	Slope
Helmholtz resonator	Backward step
Piezoelectric resonator	Transverse injection
Plasma-based actuators	Cavity
Quasi-DC discharge	Pylon

2. Physical Model and the Numerical Method

2.1. Physical Model. In this paper, a supersonic combustor with a cavity was taken as the research object [21], physically modeled as shown in Figure 1(a), with a total length of 180 mm, a designated $x = 0$ mm at its entrance, and a 1° expansion angle maintained throughout its upper wall. Upstream of the cavity, an orifice with a radius of 1 mm was injected with ethylene fuel vertically from the wall into the flow. The orifice is located 10 mm from the front edge of the cavity [22]. The length and depth of the cavity are L =56 mm and $D = 8$ mm, respectively, and the trailing edge angle is $\theta = 45\circ$.

The energy deposition distributions are designed in the streamwise direction and the spanwise direction in the simulation. They are briefly called streamwise actuation and spanwise actuation in this study. In the numerical studies, the energy depositions are modeled as cubic heating zones with a volume of $2 \times 2 \times 2\ \text{mm}^3$.The spacing of each heating zone is $L_d = 3$ mm. For the distribution in the streamwise direction, the heating zones are arranged along the centerline of the bottom wall of the combustor, downstream (position *B*), and upstream (position *C*) of the orifice. These cases are marked as case *B* and case *C*, as shown in Figure 1(b). For the distributions in the spanwise direction, the heating zones are arranged upstream (positions *D*, *E*, and *F*) or downstream (positions *G*, *H*, and *I*) of the orifice. These cases are marked as case *D*-case *I*, as shown in Figure 1(c). The scenario with no energy deposition is marked as case *A*.

The computational grid of the model is shown in Figure 2, which adopts the block-structured grids. The total number of the grids is about 3.1 million, with the wall grids intensified to ensure the thickness of the inner-layer grid is 7×10^{-7}m. The pressure far-field boundary inlet condition is used for the combustor entrance. The incoming flow has a Mach number of $Ma = 2$, a static temperature of $T_s = 823$ K, and a static pressure of $p_s = 101$ kPa. The jet orifice is set as the pressure inlet boundary condition, the total pressure at the orifice is $p_j = 0.44$ MPa, the static pressure

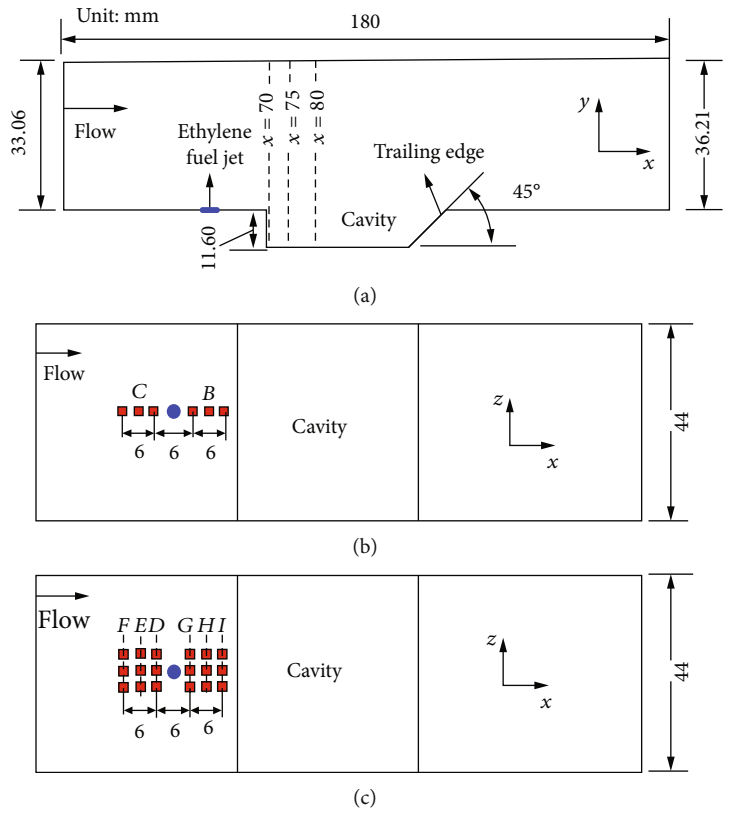

Figure 1: Schematic diagram of the physical model. (a) The physical model without energy deposition, from a side view. (b) The heating zones are arranged in the streamwise direction, from a top view. (c) The heating zones are arranged in the spanwise direction, from a top view.

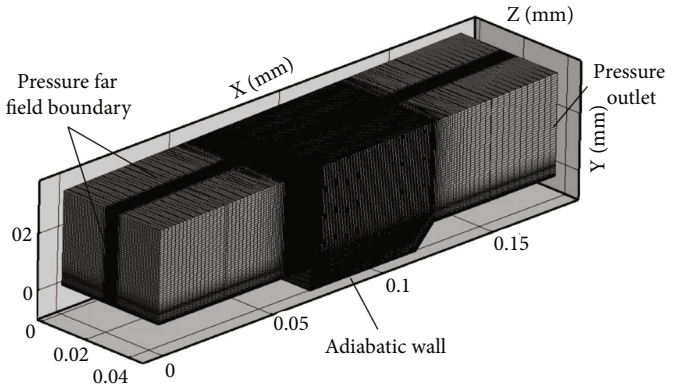

Figure 2: Computational zones and grids.

is $p_{jst} = 334\,\text{kPa}$, and the total temperature is $T_{j0} = 300\,\text{K}$. The outlet was modeled as a static pressure supersonic outlet, allowing the supersonic flow to discharge. The walls of the combustor, including the cavity, are set as no-slip adiabatic walls.

2.2. Numerical Method. In the current work, the flow fields of a supersonic combustor with and without energy deposition are simulated by solving the Reynolds-averaged N-S equations with an energy source term. The governing equation is the multicomponent, conservative N-S equation, which is expressed based on the Reynolds average in the Cartesian coordinate system as follows:

$$\frac{\partial Q}{\partial t} + \frac{\partial E}{\partial x} + \frac{\partial F}{\partial y} + \frac{\partial G}{\partial z} = \frac{\partial E_d}{\partial x} + \frac{\partial F_d}{\partial y} + \frac{\partial G_d}{\partial z} + S_p. \quad (1)$$

Q is the conserved flux. E, F, and G are the opposite flux vectors in the x, y, and z directions, respectively. t is time. S_p is the energy source term. E_d, F_d, and G_d are diffusion flux vectors in the x, y, and z directions, respectively. The

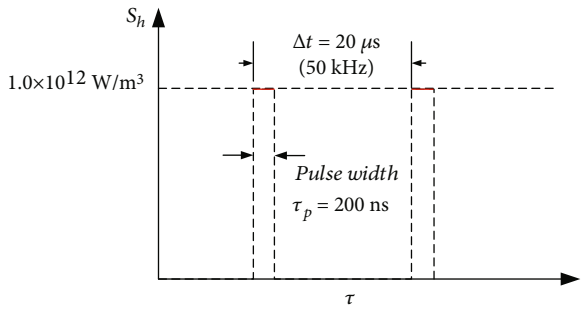

Figure 3: Schematic diagram of power density change with time as an energy source term.

detailed equations of each variable are as follows:

$$Q = \begin{bmatrix} \rho \\ \rho u \\ \rho v \\ \rho w \\ \rho e \\ \rho Y_i \end{bmatrix} E = \begin{bmatrix} \rho u \\ \rho uu + p \\ \rho uv \\ \rho uw \\ u(\rho e + p) \\ \rho u Y_i \end{bmatrix} F = \begin{bmatrix} \rho v \\ \rho vu \\ \rho vv + p \\ \rho vw \\ v(\rho e + p) \\ \rho v Y_i \end{bmatrix} G = \begin{bmatrix} \rho w \\ \rho wu \\ \rho wv \\ \rho ww + p \\ w(\rho e + p) \\ \rho w Y_i \end{bmatrix} H = \begin{bmatrix} S_{d,m} \\ S_{d,u} \\ S_{d,v} \\ S_{d,w} \\ S_{d,h} \\ w_i \end{bmatrix},$$

$$E_d = \begin{bmatrix} 0 \\ \tau_{xx} \\ \tau_{xy} \\ \tau_{xz} \\ u\tau_{xx} + v\tau_{xy} + w\tau_{xz} - q_x \\ \rho_i D_{im} \partial Y_i / \partial x \end{bmatrix} F_d = \begin{bmatrix} 0 \\ \tau_{yx} \\ \tau_{yy} \\ \tau_{yz} \\ u\tau_{xy} + v\tau_{yy} + w\tau_{yz} - q_y \\ \rho_i D_{im} \partial Y_i / \partial y \end{bmatrix} G_d = \begin{bmatrix} 0 \\ \tau_{zx} \\ \tau_{zy} \\ \tau_{zz} \\ u\tau_{zx} + v\tau_{zy} + w\tau_{zz} - q_z \\ \rho_i D_{im} \partial Y_i / \partial z \end{bmatrix}. \quad (2)$$

$i = 1, 2 \cdots$ is the total number of components. ρ is the density of the gas. ρ_i is the density of component i. u, v, and w are the velocities along the x, y, and z axis, respectively. p is pressure. e is total energy. Y_i is the mass fraction of component i. ω_i is the mass generation rate of component i. $S_{d,m}$, $S_{d,u}$, $S_{d,v}$, $S_{d,\omega}$, and $S_{d,h}$ are the source term of gaseous phase interaction and chemical reaction, and the value is 0 in the mixed flow field. τ_{ij} is the viscous stress component, and its mathematical expression is as follows:

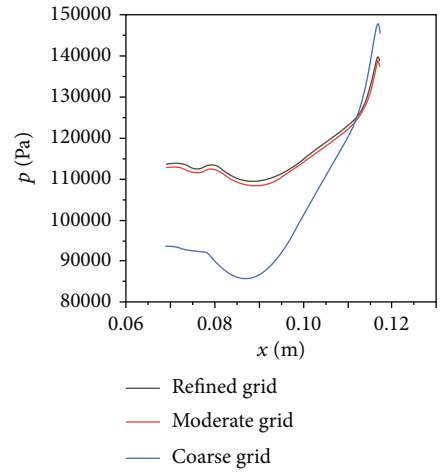

Figure 4: Wall pressure distributions in the centerline of the cavity bottom using different grids.

$$\begin{cases} \tau_{xx} = -\frac{2}{3}\mu\left(\nabla.\vec{V}\right) + 2\mu\frac{\partial u}{\partial x}, \\ \tau_{yy} = -\frac{2}{3}\mu\left(\nabla.\vec{V}\right) + 2\mu\frac{\partial u}{\partial y}, \\ \tau_{zz} = -\frac{2}{3}\mu\left(\nabla.\vec{V}\right) + 2\mu\frac{\partial u}{\partial z}, \\ \tau_{xy} = \tau_{yx} = \mu\left(\frac{\partial u}{\partial y} + \frac{\partial v}{\partial x}\right), \\ \tau_{yz} = \tau_{zy} = \mu\left(\frac{\partial w}{\partial y} + \frac{\partial v}{\partial z}\right), \\ \tau_{xz} = \tau_{zx} = \mu\left(\frac{\partial w}{\partial x} + \frac{\partial u}{\partial z}\right). \end{cases} \quad (3)$$

The subscripts x, y, and z denote partial derivatives in the x, y, and z directions, respectively. q_x, q_y, and q_z are the energy fluxes along each coordinate axis caused by heat conduction and component diffusion.

$$\begin{cases} q_x = -k\frac{\partial T}{\partial x} - \rho\sum_{i=1}^{N_s} D_{im} h_i \frac{\partial Y_i}{\partial x}, \\ q_y = -k\frac{\partial T}{\partial y} - \rho\sum_{i=1}^{N_s} D_{im} h_i \frac{\partial Y_i}{\partial y}, \\ q_z = -k\frac{\partial T}{\partial z} - \rho\sum_{i=1}^{N_s} D_{im} h_i \frac{\partial Y_i}{\partial z}. \end{cases} \quad (4)$$

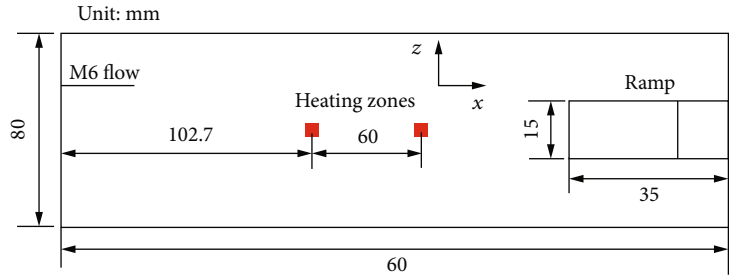

Figure 5: Schematic diagram of the physical model in reference [28].

Table 2: Parameters of the incoming flow.

Mach number M	6
Total pressure p_0	1.3 MPa
Total temperature T_0	300 K
Velocity u_∞	713 m/s
Static pressure p_∞	823.4 Pa
Static temperature T_∞	35.14 K

D_{im} is the mass diffusion coefficient of component i.

$$D_{im} = \frac{(1 - X_i)}{\sum_{i,j\neq 1} X_j / D_{ij}}. \tag{5}$$

In the above equation, X_i is the mole fraction of components. Under medium- and low-pressure conditions, the diffusion coefficient of the bicomponent mixed gas is as follows:

$$D_i = \frac{1.883 \times 10^{-2} \sqrt{T^3 \cdot (M_i + M_j)/M_i M_j}}{\rho \sigma^2{}_{ij} \Omega_D}. \tag{6}$$

In the above equation, M_i and M_j are the molecular weights of gas components i and j, respectively. σ_{ij} is the characteristic length. The thermal energy of the mixed gas can be calculated as follows:

$$e = \sum_{i=1}^{Ns} Y_i h_i + \frac{1}{2}\left(u^2 + v^2 + w^2\right) - \frac{p}{\rho}. \tag{7}$$

Enthalpy of each component is as follows:

$$h_i = h_f^0 + \int_{T_{td}}^{T} C_{p_i} dT. \tag{8}$$

The turbulence model was selected as the SST $k-\omega$ model [23], which is a combination of the near-wall Wilcox 1988 $k-\omega$ model and the separation region $k-\varepsilon$ model [24]. This model is considered for use because it predicts better free shear flow characteristics and is not sensitive to initial values. Compared with the $k-\omega$ model, this model is less sensitive to the turbulence of incoming flow. It also has better performance when calculating flow field with backpressure gradient [24]. The transport equations of k and ω are as in literature [25].

The energy deposition process can be equivalent to a Joule heating process, and this is also known as a phenomenological method. Di et al. [26] have used power density as an energy source term in the energy equation to simulate the heating process. The power density is obtained by fitting an experimental power waveform. Their numerical results match well with the experimental schlieren images, which demonstrates the effectiveness of this method in simulating the effects of energy depositions. In our simulation, a power density with a frequency of $f = 50$ kHz and a pulse width of 200 ns is used, as shown in Figure 3. Equation (9) defines the power density S_h for energy deposition [27], which is determined by the transient power $q(\tau)$, the volume of heating zones $V(x, y, z)$, and the energy conversion rate η_0. τ is the pulse width, namely. the heating time of a pulse of energy deposition. The power density of the heating zone within a single pulse is kept as $S_h = 1.0 \times 10^{12}$ W/m^3 in this study.

$$S_h = \begin{cases} \dfrac{\eta_0 Q_0}{\tau(x,y,z)} = \dfrac{q(\tau)}{V(x,y,z)}, & (x_1 < x < x_2, y_1 < y < y_2, z_1 < z < z_2, 0 < \tau < \tau_p), \\ 0, & (\text{others}). \end{cases} \tag{9}$$

In the simulation, a steady-state flow field without energy deposition (case A) is firstly obtained by a steady calculation, and then, the flow fields with energy deposition are obtained by transient calculations. The time step size was set to be 10^{-8}, and each step iterates 20 times. The flow field parameters are averaged with the data sets at different moments in 0.02 milliseconds, and they have all been converged by the average.

2.3. Grid Independence Study. The grid independence analysis is performed for the baseline case: case A. Three different grids are considered for the domain without energy deposition, with 0.9, 3.1, and 6.9 million cells, which are coarse, medium, and refined grids. The local wall pressure distribution along the centerline of the bottom wall of the cavity is monitored, as shown in Figure 4. It can be seen that there is no remarkable difference between the results with medium and refined grids, while the coarse grid leads to a large deviation. The good agreement found in pressure distributions between the medium and fine grids justified the selection

(a) (b)

Figure 6: Comparison of the experimental schlieren image and the numerical density gradient contour. (a) The experimental schlieren image. (b) The density gradient contour using the current numerical method.

of the medium grid for the rest of the study, to improve the computational accuracy and efficiency.

2.4. Simulation Validation. It is necessary to validate the reliability of our simulation from different aspects. The verification for simulating the heating effects of energy deposition on a supersonic flow is performed by comparing our numerical schlieren image with the experimental one in reference [28]. In this reference, the experiment was conducted in a $Ma = 6$ wind tunnel, and the schematic diagram of the test model is shown in Figure 5. Our verification example and the corresponding incoming flow parameters, presented in Table 2, are both taken the same as those in this reference.

As shown in Figure 6, the density gradient contour on the symmetry plane of the model obtained by the current numerical method agrees well with the experimental schlieren image. The consistencies are found in shock wave structures, the shear layer, and the position of the reattachment shock. These consistencies indicate that the current numerical method can well simulate the flow field with the heating due to plasma energy deposition.

Quantitative verification is also performed using a supersonic combustor model with a cavity [29]. The verification example and the corresponding incoming flow parameters are both taken the same as those in this reference. As shown in Figure 7, the pressure distribution at the trailing edge of the cavity, obtained by the current numerical method, matches well with experimental data in this reference. This indicates that the numerical method can accurately simulate the flow in a supersonic combustor with a cavity.

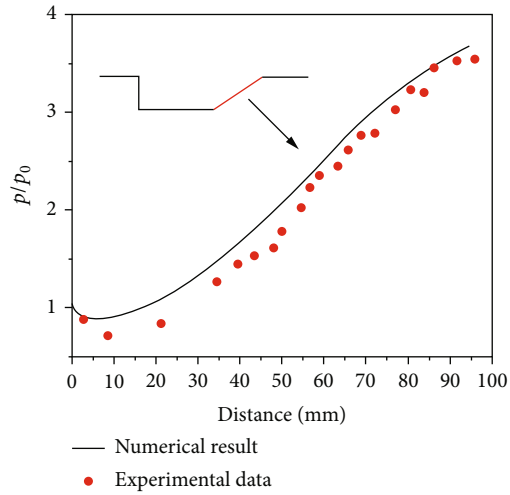

Figure 7: Comparison of the numerical wall pressure distribution with the experimental data.

3. Results and Discussion

3.1. Effects of the Streamwise Actuation on the Fuel Mixing. Figure 8 shows the mass fraction contours of the ethylene components and the corresponding streamlines for case *A*, case *B*, and case *C*, at planes of $x = 70$, 75, and 80 mm under the cold flow. All the selected planes are located near the cavity. Clipped regions with a mass fraction scope $Y_{C2H4} \geq 0.15$ are displayed. As can be seen from the figure, the ethylene jet evolves into typical vortex structures in the supersonic flow, thus facilitating the fuel mixing with the supersonic flow. Figure 8(a) shows that in each case, a large-scale counter-rotating vortex pair (CVP) is formed due to the interaction between the mainstream and the jet, with the majority of ethylene components being transported to this region. At the plane of $x = 70$ mm, the ethylene component has a similarly high concentration in all cases, while the ethylene diffusion is much greater in case *B* and case *C*. The jet plume develops downstream and diffuses in a direction perpendicular to the wall. The scale of the vortex in case *B* and case *C* is larger than that in case *A*. At the plane of $x = 75$ mm, as shown in Fig. 8(b), the ethylene component still has a high-concentration zone, while it decayed significantly in case *B* and case *C*. Meanwhile, an expansion towards the z direction occurs in the ethylene component, which is significant in case *B* and case *C*. In comparison, case *B* has the largest CVP among the three cases. These contours suggest that the high-concentration zone of the ethylene component is related to the location of the CVP, and the scale of CVP affects the degree of the diffusion of the component. With the addition of heating, the development of CVP is promoted, resulting in a vortex with a larger scale, and this helps to enhance fuel mixing.

The mixing efficiency η_{mix} of the fuel can be acquired by equations (10) and (11) [30], where α represents the mass fraction of the fuel, α_{react} represents the mass fraction when the fuel is just ready to react chemically, and α_{atoich} represents the mass fraction when the equivalence ratio of the fuel equals to $\Phi = 1$. For the ethylene, $\alpha_{atoich} = 0.0635$. Another way to measure the mixing degree is by using the maximum concentration decay curve [25], which describes the maximum ethylene concentration α_{max} change versus the flow

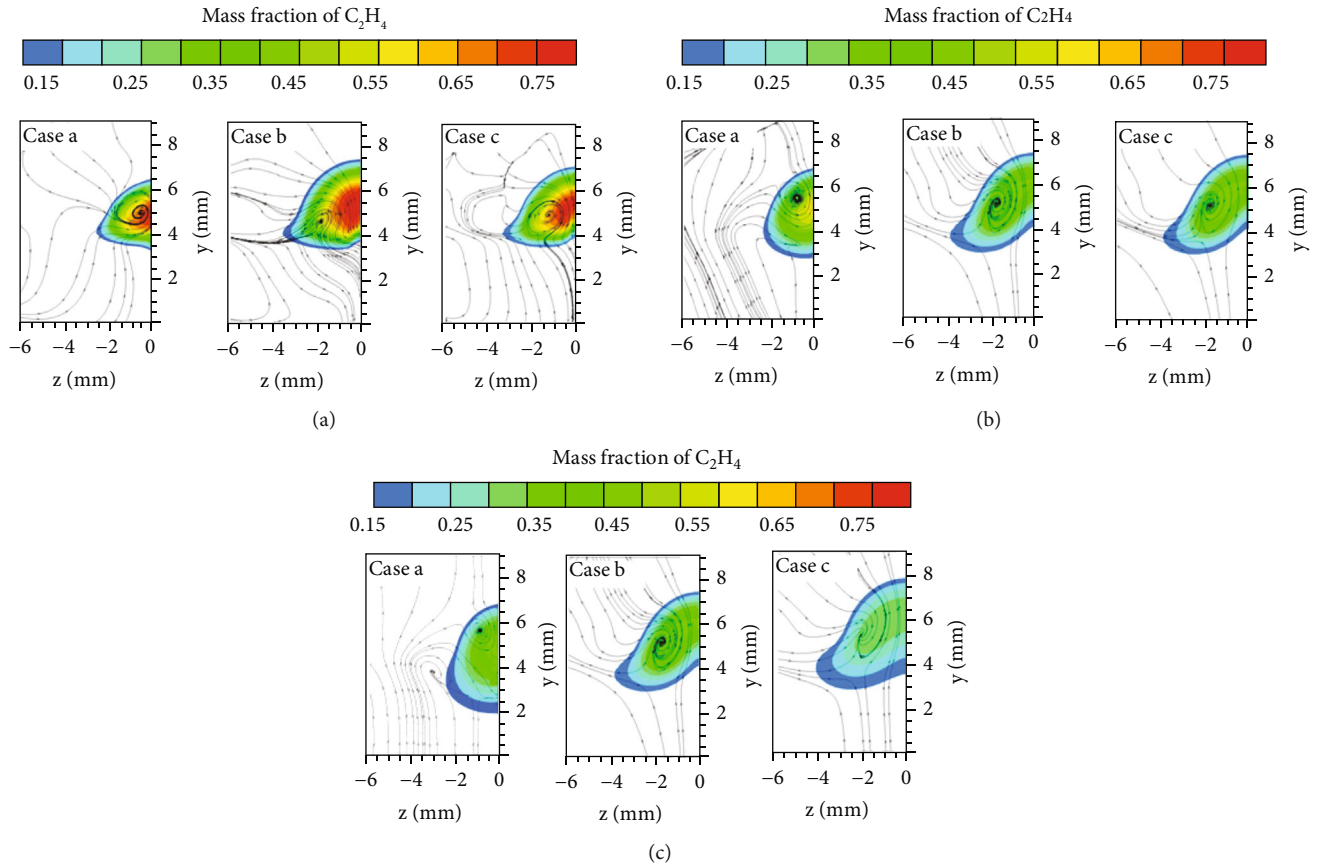

FIGURE 8: Mass fraction contours of the ethylene component and the streamlines at $x = 70$, 75, and 80 mm for case A, case B, and case C. (a) $x = 70$ mm. (b) $x = 75$ mm. (c) $x = 80$ mm.

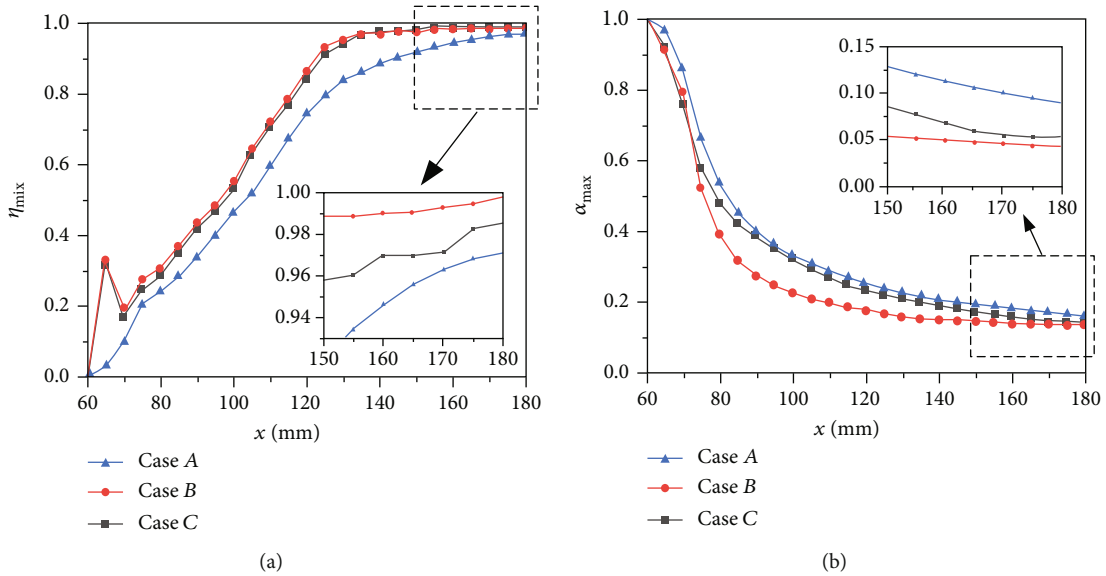

FIGURE 9: Mixing efficiency of ethylene (a) and the corresponding maximum concentration decay curve (b) in case *A* without actuation and case *B*-case *C* with streamwise actuation.

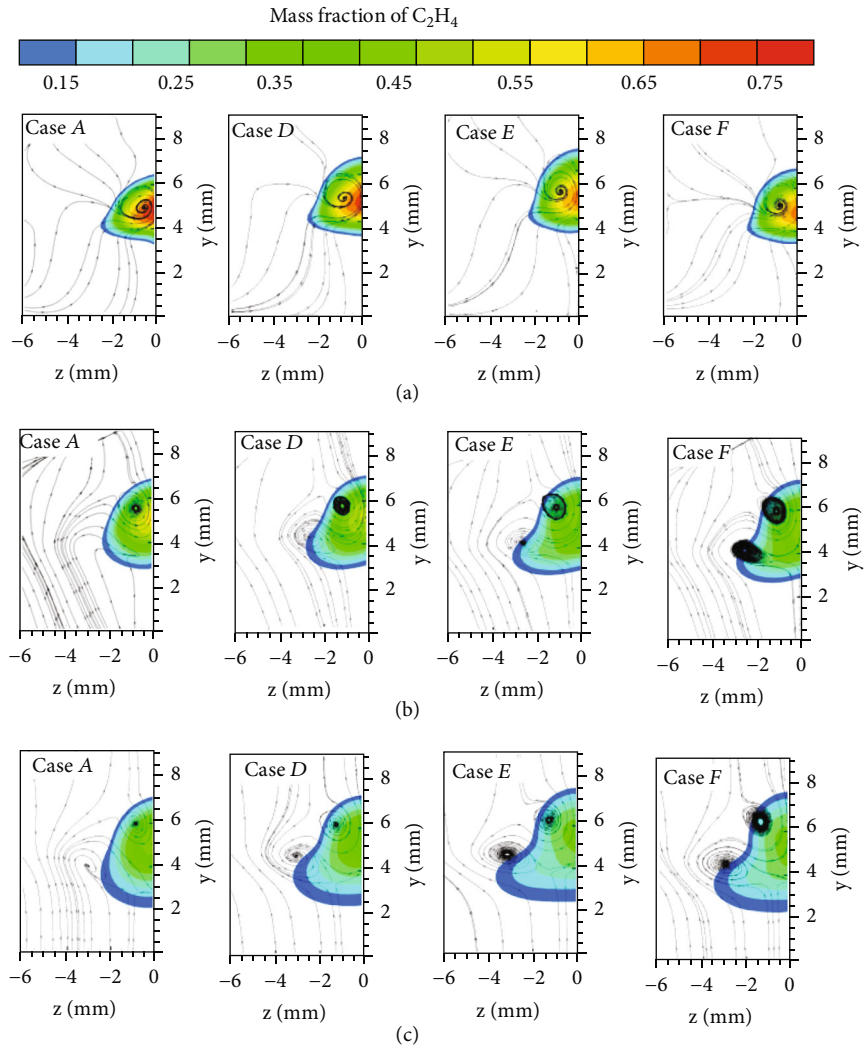

Figure 10: Mass fraction contour and streamline diagram of case A and cases D-F at different planes. (a) $x = 70$ mm. (b) $x = 75$ mm. (c) $x = 80$ mm.

distance.

$$\eta_{\text{mix}} = \frac{\dot{m}_{\text{fuel,mixed}}}{\dot{m}_{\text{fuel,total}}} = \frac{\int \alpha_{\text{react}} \rho \mu dA}{\int \alpha \rho \mu dA}, \tag{10}$$

$$\alpha_{\text{react}} = \begin{cases} \alpha (\alpha \le \alpha_{\text{atoich}}), \\ \dfrac{\alpha_{\text{atoich}}(1-\alpha)}{1-\alpha_{\text{atoich}}} (\alpha \ge \alpha_{\text{atoich}}). \end{cases} \tag{11}$$

The mixing efficiency and the maximum concentration decay curves are shown in Figure 9. As can be seen from Figure 9(a), the mixing efficiency for each case follows the same trend: from $x = 60$ mm to $x = 80$ mm, there is a sudden increase in the mixing efficiencies in case B and case C with energy depositions, because the rapid heating due to the energy deposition exerts a strong disturbance on the jet plume. Compared to case A, case B and case C have a higher mixing efficiency. At the outlet of the model, the mixing efficiency for each case increases close to $\eta_{\text{mix}} = 1.0$, the mixing efficiency for case B and case C is 2.7% and 1.47% higher than case A, respectively. This indicates that the streamwise actuation can enhance ethylene mixing efficiency, and this can be explained by the CVP expansion found above. As can be seen from Figure 9(b), the corresponding maximum concentration magnitude ranks as follows: case A>case C>case B. At the combustor outlet, the maximum concentration in case B and case C is 52% and 40% lower than that of case A, respectively. These results indicate that it is more conducive to fuel mixing when the streamwise actuation is located downstream of the orifice, and this is closely related to the larger CVP that makes the ethylene dispersed more significantly. The CVP is larger in case B and case C, probably because the heating gas disturbance directly acts on the jet plume.

3.2. Effects of the Spanwise Actuation on the Fuel Mixing. Figure 10 shows the mass fraction contour of ethylene and the corresponding streamline for case A and cases D-F at planes of $x = 70$, 75, and 80 mm. As can be seen from this figure, the ethylene jet also evolves into streamwise vortex structures in the supersonic flow. For these cases, the CVP

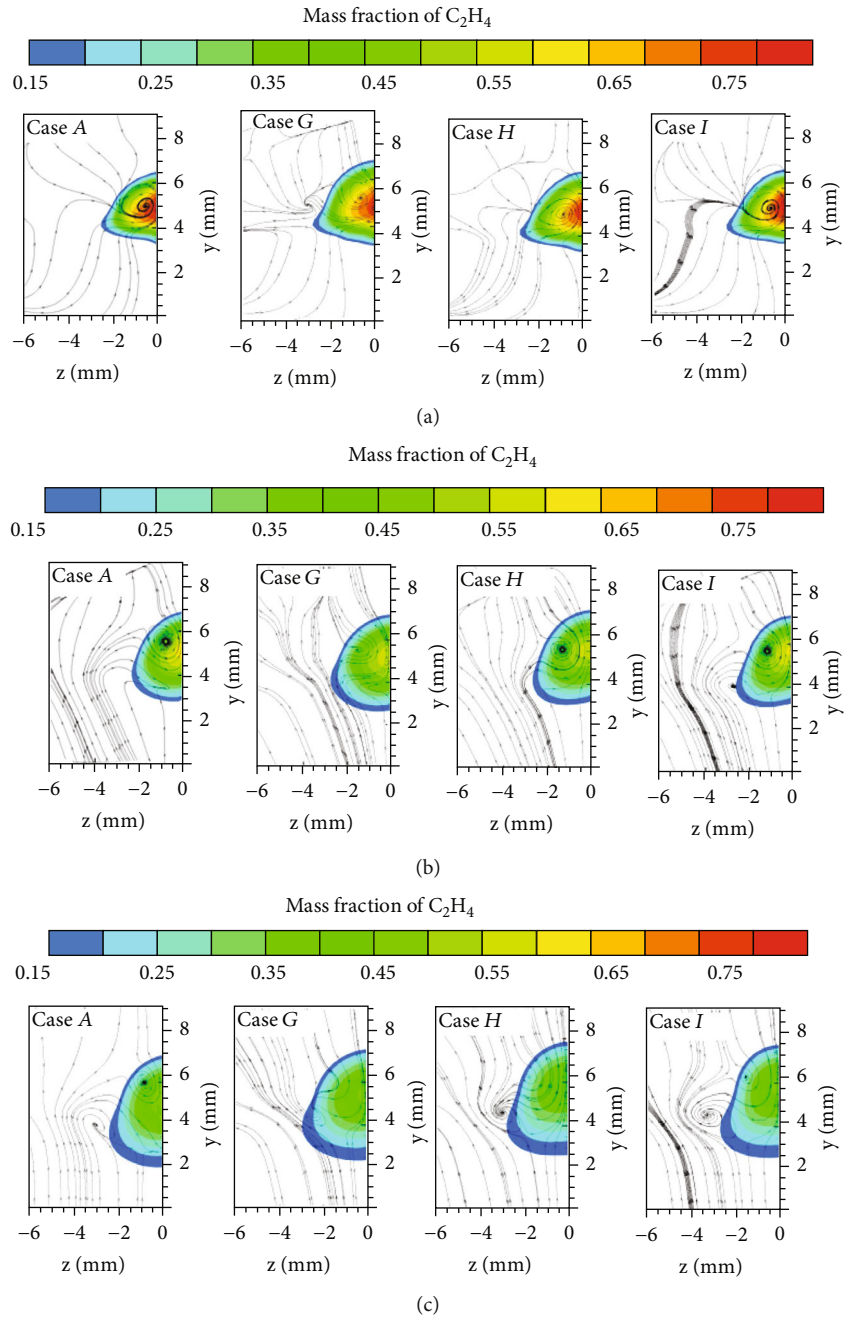

Figure 11: Mass fraction contour and streamline of case *A* and cases *G-I* at different planes. (a) $x = 70$ mm. (b) $x = 75$ mm. (c) $x = 80$ mm.

seems to be strengthened by the upstream disturbances; moreover, another counter-rotating vortex pair (CVP-1) is induced beneath the CVP. Affected by the interaction between the CVP and CVP-1, the ethylene component presents a "pear-shaped" distribution. At $x = 70$ mm, the distributions of these four cases are similar. The maximum concentration of fuel ranks as follows: case *A*>case *D*>case *E*>case *F*. At $x = 75$ mm, as shown in Figure 10(b), the maximum ethylene concentration is decreased significantly, and the ethylene is dispersed towards the z direction under the energy deposition. This is because of the larger CVP and CVP-1 induced in cases *D-F*. Figure 10(c) shows that at $x = 80$ mm, the maximum concentration of the ethylene component for these cases is nearly the same, but the fuel dispersal is even more prominent under the actuation. It can be seen that the spanwise actuation upstream of the orifice makes the fuel concentrate in a "pear-shaped" region due to the interaction between the CVP and CVP-1. The vortexes introduced by the energy deposition can also expand the fuel distribution scope and promote fuel diffusion, resulting in an improvement in the mixing efficiency.

Figure 11 shows the mass fraction contour of ethylene and the corresponding streamline for case *A* and cases *G-I* at planes of $x = 70$, 75, and 80 mm. At $x = 70$ mm, as shown in Figure 11(a), the distribution of the ethylene components in these four cases is nearly the same. The maximum

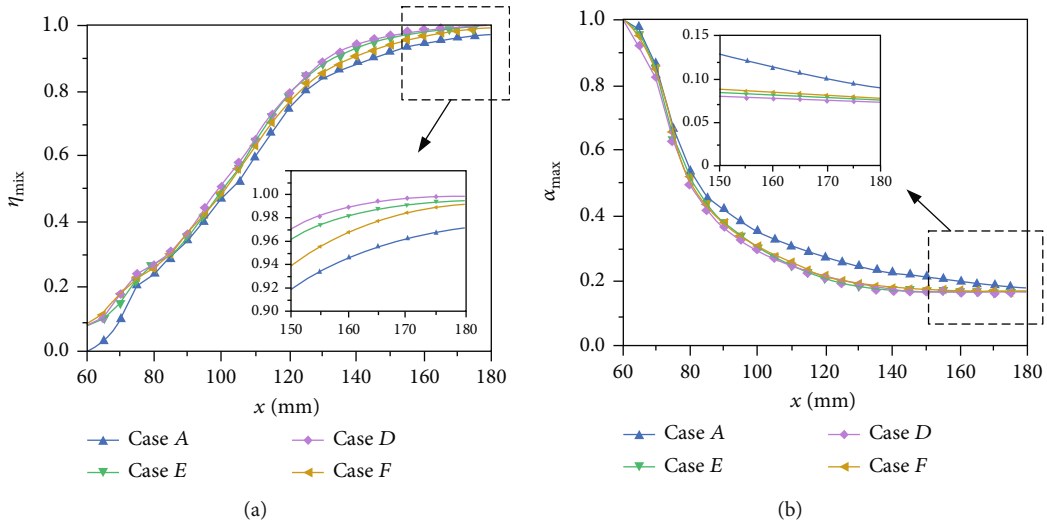

Figure 12: Mixing efficiency of ethylene (a) and the corresponding maximum concentration decay curve (b) in case A without actuation and cases D-F with spanwise actuation upstream of the orifice.

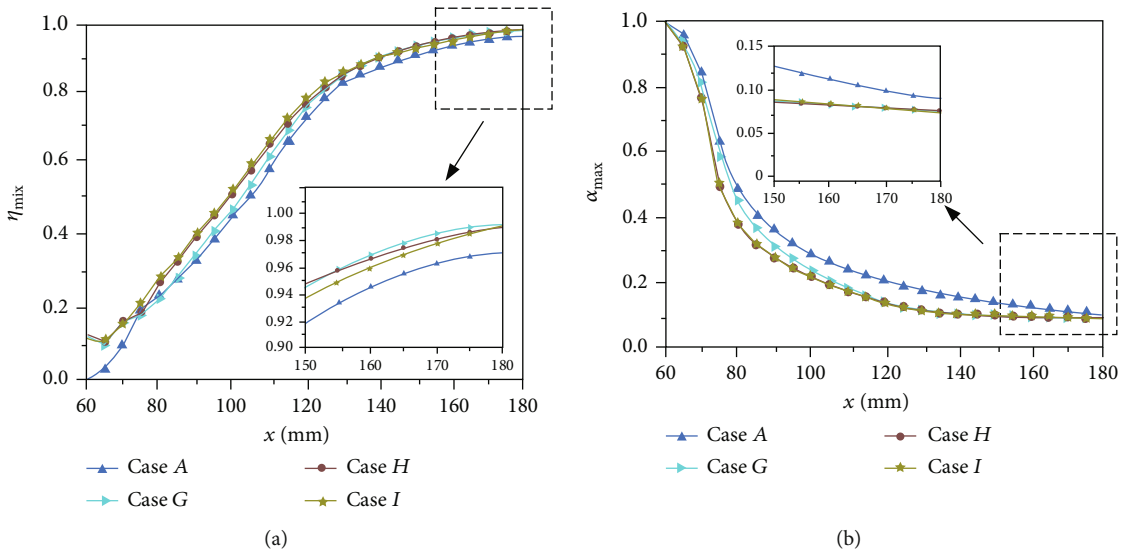

Figure 13: Mixing efficiency of ethylene (a) and the corresponding maximum concentration decay curve (b) in case A without actuation and case G-case I with spanwise actuation downstream of the orifice.

component concentration ranks as follows: case A>case I>case H>case G. A CVP-1 is induced in case G. Figure 11(b) shows that, at $x = 75$ mm, the fuel distribution in these four cases is similar, but the maximum concentration in the core area of CVP is slightly decreased under actuation. The CVP-1also appears in case I and case G. At $x = 80$ mm, as shown in Figure 11(c), the ethylene distribution evolves into a "pear-shaped" one for all cases. The CVP-1 in case H and case I is dominant, which may play a key role in fuel mixing. However, case G has a smaller CVP-1. It can be seen that the spanwise actuation downstream of the orifice can also promote fuel diffusion and extend the ethylene distribution scope, but this effect is not very satisfactory. From what has been described above, it can be found that the energy deposition in the centerline contributes to the formation of CVP, while the one off the centerline contributes to the formation of CVP-1.

The mixing efficiency and the maximum concentration decay curve for each case with spanwise actuation upstream of the jet orifice are, respectively, shown in Figure 12. It can be seen from Figure 12(a) that, compared with case A, the mixing efficiency for the three cases under actuation is larger, and so is the maximum concentration decay rate. At the exit of the combustor, the mixing efficiency for case D is 1.40% higher than that of case A and 1.35% for case E and 1.36% for case F. This indicates that the spanwise actuation enhances the mixing of ethylene. As can be seen from Figure 12(b), there is little difference in the maximum

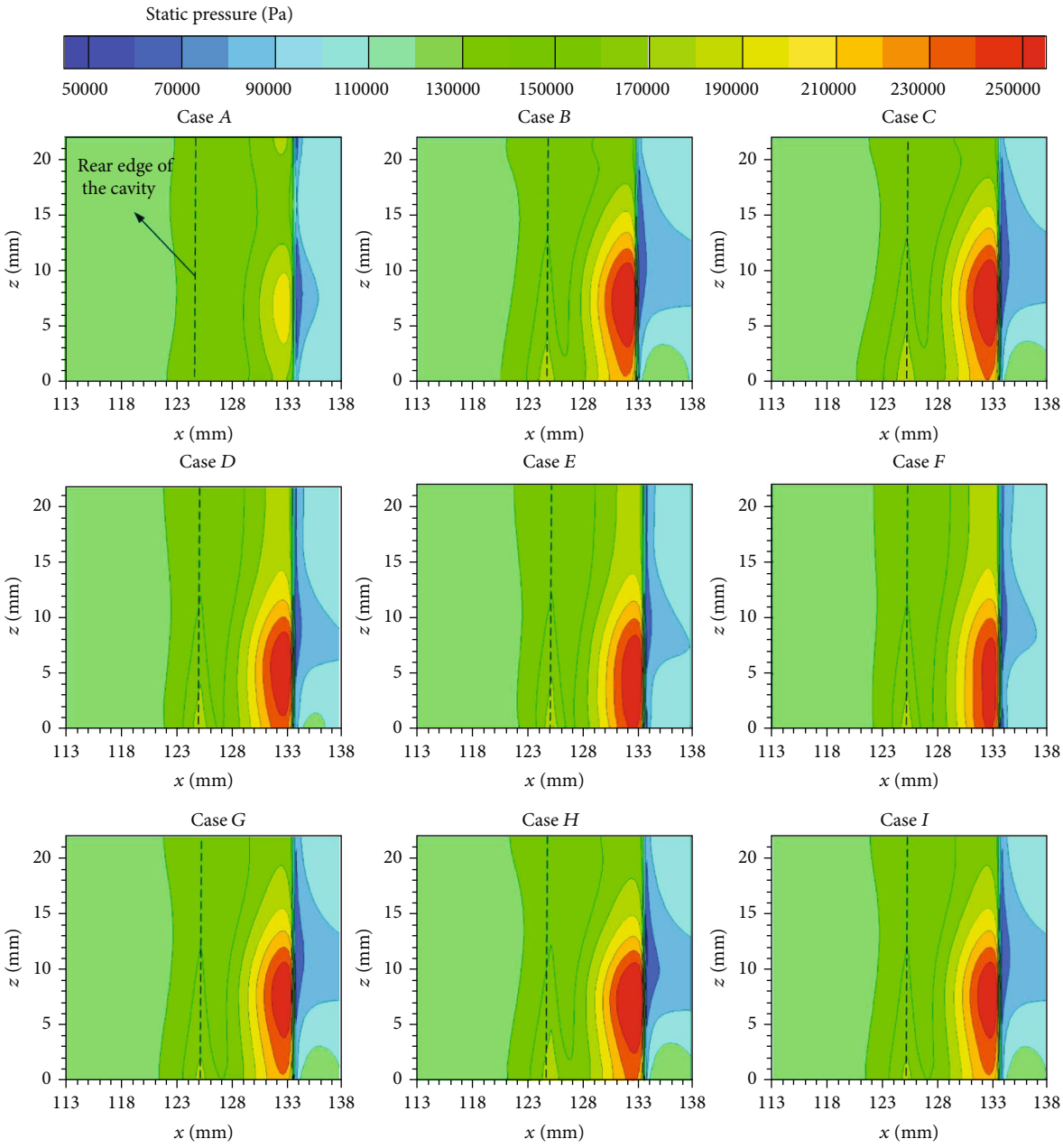

Figure 14: Wall pressure contours near the trailing edge of the cavity of all cases.

Table 3: Total pressure recovery coefficients.

Case	Case *A*	Case *B*	Case *C*	Case *D*	Case *E*	Case *F*	Case *G*	Case *H*	Case *I*
η	0.8713	0.8659	0.8658	0.8643	0.8612	0.8637	0.8615	0.8645	0.8623

concentration at the exit of the combustor for the cases with actuation. It is decreased by 18.7% for case *D*, in comparison with that in case *A* and 16.5% for case *E* and 16.6% for case *F*.

For cases with spanwise actuation downstream of the jet orifice. Figure 13(a) shows that the mixing efficiency with actuation is also improved, in comparison with case *A*. At the exit of the combustor, the mixing efficiency of case *G* is 1.15% higher than that of case *A* and 0.92% for case *H* and 1.02% for case *I*. Although the mixing efficiency increases in these cases, it is lower than that in cases *D*-*F*. As shown in Figure 13(b), there is almost no difference in the maximum concentration at the exit of the combustor for the cases with actuation. For cases *G*-*I*, it decreases by nearly 18% in comparison with that in case *A*.

From the above analysis, the spanwise actuation upstream of the orifice has a better mixing effect than that downstream of the orifice. Moreover, the energy deposition closer to the jet orifice has a better mixing effect. However, the mixing efficiencies of the cases with spanwise actuation are lower than those of cases with streamwise actuation. This is probably because although the energy deposition off the centerline induces CVP-1, it decays the entrainment ability of the main CVP due to their opposite rotating directions. On the other hand, the strong disturbances off the centerline could not completely act on the jet plume.

3.3. Effect of the Energy Deposition on the Total Pressure Recovery of the Combustor. Figure 14 shows the wall pressure contours from a top view. It can be seen that there are high-pressure areas on the trailing edge of the cavity because of the impact from the shear layer within the cavity. The pressure peaks are increased for the cases with actuation compared with case *A*. This is because the incoming flow is blocked by the heating zones in the centerline, which is known as the "thermal choking" effect. This results in a velocity/momentum increase in the fluids on either side of the jet plume, and this enhances the impact on the trailing edge.

The total pressure recovery coefficient is one of the important indexes for measuring combustor performance. The higher the total pressure recovery coefficient is, the stronger the combustor outlet flow works. The definition of the total pressure recovery coefficient is given in equation (12) [31], where $\bar{P}_0$ is the total pressure of the combustor, which is defined by equation (13) [32], u is the flow velocity across the y - z plane, and ρ is the corresponding density. The coefficient for each case is calculated, listed in Table 3. The results suggest that the coefficient decreases to some extent as the energy deposition is added into the flow. Although the addition of energy deposition will bring a certain total pressure loss, it is not significant.

$$\eta = \frac{\bar{P}_{0\_\text{out}}}{\bar{P}_{0\_\text{in}}}, \tag{12}$$

$$\bar{P}_0 = \frac{\int P_0 \rho u dA}{\int \rho u dA}. \tag{13}$$

4. Conclusions

This paper proposes a method to improve the mixing efficiency of a supersonic combustor by using arrayed pulsed energy depositions. The effects of the energy deposition in various distributions, upstream or downstream of the jet orifice, on the fuel mixing are compared. The numerical method is firstly validated by comparing the numerical results with previous experimental data, and it is found that this method can well simulate the energy effects on the supersonic flow. The main findings regarding the effects of the energy deposition are as follows:

(1) The mixing efficiency of the ethylene fuel can be improved as the energy deposition is activated, either upstream or downstream of the jet orifice. Compared with the cases with spanwise actuation, the energy deposition arranged in the streamwise direction and downstream of the jet orifice leads to a significant improvement in the mixing efficiency and maximum concentration decay rate of the ethylene fuel. This is because the scale of the jet-induced counter-rotating vortex pair is increased by the energy deposition, and this case is proved to be the most effective in the mixing enhancement. In this case, the mixing efficiency at the combustor outlet is increased by 2.7%, in comparison with the baseline case

(2) With the addition of the energy deposition, the pressure on the trailing edge of the cavity is found to be increased due to a stronger impact from the shear layer flow. This leads to a total pressure recovery decrease. However, this decrease is not significant for the cases with energy depositions

Data Availability

The data used to support the findings of this study are available from the corresponding author upon request.

Conflicts of Interest

The authors declare no conflict of interest.

Acknowledgments

This study is supported by the National Natural Science Foundation of China (Grant No. 12002363) and the National Key R&D Program of China (Grant No. 2019YFA0405300).

References

[1] Q. Tu, H. Takahashi, and C. Segal, "Effects of pylon-aided fuel injection on mixing in a supersonic flowfield," in *Proceedings of the 48th AIAA Aerospace Sciences Meeting Including the New Horizons Forum and Aerospace Exposition*, Florida, 2010.

[2] Z. W. Huang, G. Q. He, F. Qin, and X. G. Wei, "Large eddy simulation of flame structure and combustion mode in a hydrogen fueled supersonic combustor," *International Journal of Hydrogen Energy*, vol. 40, no. 31, pp. 9815–9824, 2015.

[3] L. Li, W. Huang, L. Yan, S. Li, and L. Liao, "Mixing improvement induced by the combination of a micro-ramp with an air porthole in the transverse gaseous injection flow field," *International Journal of Heat and Mass Transfer*, vol. 124, pp. 109–123, 2018.

[4] G. Choubey, Y. Deuarajan, W. Huang, K. Mehar, M. Tiwari, and K. M. Pandey, "Recent advances in cavity-based scramjet engine- a brief review," *International Journal of Hydrogen Energy*, vol. 44, no. 26, pp. 13895–13909, 2019.

[5] G. Choubey, Y. Devarajan, W. Huang, A. Shafee, and K. M. Pandey, "Recent research progress on transverse injection technique for scramjet applications-a brief review," *International Journal of Hydrogen Energy*, vol. 45, no. 51, pp. 27806–27827, 2020.

[6] W. Huang, Z. G. Wang, J. P. Wu, and S. B. Li, "Numerical prediction on the interaction between the incident shock wave and the transverse slot injection in supersonic flows," *Aerospace Science and Technology*, vol. 28, no. 1, pp. 91–99, 2013.

[7] W. Huang, S. B. Li, L. Yan, and Z. G. Wang, "Performance evaluation and parametric analysis on cantilevered ramp injector in supersonic flows," *Acta Astronautica*, vol. 84, pp. 141–152, 2013.

[8] F. Vergine, M. Crisanti, L. Maddalena, V. Miller, and M. Gamba, "Supersonic combustion of pylon-injected hydrogen in high-enthalpy flow with imposed vortex dynamics," *Journal of Propulsion and Power*, vol. 31, no. 1, pp. 89–103, 2015.

[9] A. Ben-Yakar, *Experimental Investigation of Mixing and Ignition of Transverse Jets in Supersonic Crossflows*, Stanford University, 2001.

[10] T. Mathur, M. Gruber, K. Jackson et al., "Supersonic combustion experiments with a cavity-based fuel injector," *Journal of Propulsion & Power*, vol. 17, no. 6, pp. 1305–1312, 2001.

[11] S. Leonov, Y. Isaenkov, D. Yarantsev, and M. Schneider, "Fast mixing by pulse discharge in high-speed flow," in *Proceedings of the Aiaa/ahi Space Planes & Hypersonic Systems & Technologies Conference*, Canberra, Australia, 2013.

[12] S. B. Leonov, A. Houpt, and B. Hedlund, "Experimental demonstration of plasma-based flameholder in a model scramjet," in *21st AIAA International Space Planes and Hypersonics Technologies Conference*, p. 2249, Xiamen, China, 2017.

[13] A. Houpt, S. Gordeyev, T. J. Juliano, and S. B. Leonov, "Optical measurement of transient plasma impact on corner separation in M=4.5 airflow," in *Proceedings of the Aiaa Aerospace Sciences Meeting*, San Diego, California, USA, 2016.

[14] J. Shi, Y. Hong, G. Bai, and L. Ke, "Effect of thermal actuator on vortex characteristics in supersonic shear layer," in *Proceedings of the 47th AIAA Fluid Dynamics Conference*, Denver, Colorado, 2017.

[15] T. Ombrello, C. Carter, J. Mccall et al., "Enhanced mixing in supersonic flow using a pulse detonator," *Journal of Propulsion and Power*, vol. 31, no. 2, pp. 654–663, 2015.

[16] F. Rogg, M. Bricalli, S. O'Byrne, A. S. Pudsey, and P. Marzocca, "Mixing enhancement in a hydrocarbon-fuelled scramjet engine through repeated laser sparks," in *Proceedings of the 23rd AIAA International Space Planes and Hypersonic Systems and Technologies Conference*, Montreal, Quebec, Canada, 2020.

[17] A. A. Zheltovodov and E. A. Pimonov, "The effect of localized pulse-periodic energy supply on supersonic mixing in channels," *Technical Physics Letters*, vol. 43, no. 8, pp. 739–741, 2017.

[18] F. Liu, H. Yan, and A. A. Zheltovodov, "Mixing enhancement by pulsed energy deposition in jet/shock wave interaction," *AIAA Journal*, vol. 59, no. 7, pp. 2467–2477, 2021.

[19] G. Song, J. Li, and M. Tang, "Direct numerical simulation of the pulsed arc discharge in supersonic compression ramp flow," *Journal of Thermal Science*, vol. 29, no. 6, pp. 1581–1593, 2020.

[20] M. Tang, Y. Wu, S. Guo, Z. Sun, and Z. Luo, "Effect of the streamwise pulsed arc discharge array on shock wave/boundary layer interaction control," *Physics of Fluids*, vol. 32, no. 7, article 076104, 2020.

[21] S. Zhou, W. Nie, and X. Che, "Numerical investigation of influence of quasi-DC discharge plasma on fuel jet in scramjet combustor," *IEEE Transactions on Plasma Science*, vol. 43, no. 3, pp. 896–905, 2015.

[22] G. Choubey and K. M. Pandey, "Effect of different wall injection schemes on the flow-field of hydrogen fuelled strut-based scramjet combustor," *Acta Astronautica*, vol. 145, pp. 93–104, 2018.

[23] W. Huang, J. G. Tan, J. Liu, and L. Yan, "Mixing augmentation induced by the interaction between the oblique shock wave and a sonic hydrogen jet in supersonic flows," *Acta Astronautica*, vol. 117, pp. 142–152, 2015.

[24] W. Huang, W. D. Liu, S. B. Li, Z. X. Xia, J. Liu, and Z. G. Wang, "Influences of the turbulence model and the slot width on the transverse slot injection flow field in supersonic flows," *Acta Astronautica*, vol. 73, pp. 1–9, 2012.

[25] C. Segal, *The Scramjet Engine : Processes and Characteristics*, Cambridge University Press, 2010.

[26] J. Di, C. Wei, Y. Li et al., "Characteristics of pulsed plasma synthetic jet and its control effect on supersonic flow," *Chinese Journal of Aeronautics*, vol. 11, 2015.

[27] S. Haack, T. Taylor, J. Emhoff, and B. Cybyk, "Development of an analytical sparkjet model," in *Proceedings of the Flow Control Conference*, Chicago, Illinois, 2013.

[28] H. Wang, F. Xie, J. Li, C. Yao, and Y. Yang, "Study on control of hypersonic aerodynamic force by quasi-DC discharge plasma energy deposition," *Acta Astronautica*, vol. 187, pp. 325–334, 2021.

[29] C. C. Horstman, G. S. Settles, S. M. Bogdanoff, and D. R. Williams, "A reattaching free shear layer in compressible turbulent flow-a comparison of numerical and experimental results," in *19th Aerospace Sciences Meeting*, St. Louis,-MO,U.S.A., 1981.

[30] S. Majumdar, *Turbulence Modeling for CFD, Part 2*, In its CFD: Advances and Applications, 1994.

[31] N. N. Fedorova, I. A. Fedorchenko, M. A. Goldfeld, and Y. V. Zakharova, "Mathematical modeling of supersonic flow over open cavity with mass supply," in *Proceedings of the V European Conference on Computational Fluid Dynamics ECCOMAS CFD*, Lisbon, Portugal, 2010.

[32] A. Rajasekaran and V. Babu, "Numerical simulation of three-dimensional reacting flow in a model supersonic combustor," *Journal of Propulsion and Power*, vol. 22, no. 4, pp. 820–827, 2006.